Chemical Science

ROYAL SOCIETY OF CHEMISTRY

EDGE ARTICLE

View Article Online
View Journal | View Issue

Cite this: *Chem. Sci.*, 2023, **14**, 11490

All publication charges for this article have been paid for by the Royal Society of Chemistry

Received 10th July 2023
Accepted 30th September 2023

DOI: 10.1039/d3sc03508e

rsc.li/chemical-science

Synthesis, supramolecular aggregation, and NIR-II phosphorescence of isocyanorhodium(I) zwitterions†

Wenxuan Wei,[a] Jun Wang,*[b] Xiaomei Kang,[a] Haoquan Li,[a] Qun He,[a] Guanjun Chang [c] and Weifeng Bu *[ad]

Development of new second near-infrared (NIR-II, 1000–1700 nm) luminophores is highly desirable, and d^8 square-planar metal complexes with NIR-II phosphorescence have been rarely reported. Herein, we explore an asymmetric coordination paradigm to achieve the first creation of NIR-II phosphorescent isocyanorhodium(I) zwitterions. They show a strong tendency for aggregation in solution, arising from close Rh(I)···Rh(I) contacts that are further intensified by π–π stacking interactions and the hydrophilic–hydrophobic effect. Based on such supramolecular aggregation, zwitterions **2** and **5** are found to yield NIR-II phosphorescence emissions centered at 1005 and 1120 (1210, shoulder) nm in methanol–water mixed solvents, respectively. These two bands show red shifts to 1070 and 1130 (1230, shoulder) nm in the corresponding polymer nanoparticles in water. The resulting polymer nanoparticles can brighten *in vivo* tumor issues in the NIR-II region with a long-circulating time. In view of the synthetic diversity established by the asymmetric coordination paradigm, this work provides an extraordinary opportunity to explore NIR-II luminophores.

Introduction

Supramolecular self-assembly of square-planar d^8 metal complexes has become a promising approach to create functional nanomaterials due to their rich luminescence properties and interesting self-assembly behaviors driven by directional metal···metal interactions arising from the close proximity of the metal centers.[1] To date, the reports on d^8 metal complexes have mainly focused on Pt(II),[2] Pd(II)[3] and Au(III) complexes,[4] and their luminescence ranges are mainly distributed in the visible (380–700 nm) and first near-infrared window (NIR-I, 700–950 nm). However, d^8 metal complexes with second near-infrared window (NIR-II, 1000–1700 nm) phosphorescence have been rarely reported in the present stage. Such luminophores are of fundamental importance for their promising applications in bioimaging,[5] telecommunications,[6] and optoelectronics.[7]

Homoleptic tetrakis(isocyanido)rhodium(I) complexes with a d^8 electronic configuration, $[Rh(C{\equiv}NR)_4]^+X^-$ (R = alkyl or aryl; X^- = counter-anions), display a strong tendency to aggregate into dimers, trimers, and oligomers in a cofacial manner in concentrated solutions, and are typically driven by extended Rh(I)···Rh(I) and π–π stacking interactions.[4b,8] Isocyanidorhodium(I) complexes exhibit monomeric emissions in the range of 510–588 nm,[8f,h] and their dimeric emissions are found to be red-shifted to the range of 656–714 nm.[9] Interestingly, $[Rh(C{\equiv}N\text{-}2,6\text{-xylyl})_4]^+$ based nanowires[8e] and nanomicelles,[10] wherein trimeric and/or higher aggregates form, show intense NIR luminescence centered at 806 and 940 nm in water, respectively. This increasingly red-shifting tendency in the emission bands, encourages us to create NIR-II luminescent isocyanidorhodium(I) complexes. Unfortunately, rhodium(I) isocyanide complexes having NIR-II luminescence are not yet identified so far, likely due to their immutable, symmetric coordination mode[8] and thus innate limitation in molecular diversity.

Herein, we report the first creation of zwitterionic isocyanorhodium(I) complexes with an asymmetric coordination paradigm (**1–6**, Scheme 1) and their NIR-II luminescence properties. These asymmetric zwitterions show a high aggregation tendency in solution, stemming from extended Rh(I)···

[a]*Key Laboratory of Nonferrous Metals Chemistry and Resources Utilization of Gansu Province, State Key Laboratory of Applied Organic Chemistry, College of Chemistry and Chemical Engineering, Lanzhou University, Lanzhou, 730000, China. E-mail: buwf@lzu.edu.cn*

[b]*Hunan Province Cooperative Innovation Center for Molecular Target New Drug Study, School of Pharmaceutical Science, Hengyang Medical School, University of South China, Hengyang, 421001, China. E-mail: wangjun@usc.edu.cn*

[c]*State Key Laboratory of Environment-Friendly Energy Materials & School of Material Science and Engineering, Southwest University of Science and Technology, Mianyang, 621010, China*

[d]*State Key Laboratory of Solid Lubrication, Lanzhou Institute of Chemical Physics, Chinese Academy of Sciences, Lanzhou, 730000, China*

† Electronic supplementary information (ESI) available: Synthesis and characterization of asymmetric arylisocyanidorhodium(I) zwitterions, additional ^{1}H NMR spectra, UV–vis absorption and emission spectra; additional TEM images, and DLS and WAXS plots. Cytotoxicity of various cells treated with **2-PN** and **5-PN**; and H&E staining images. See DOI: https://doi.org/10.1039/d3sc03508e

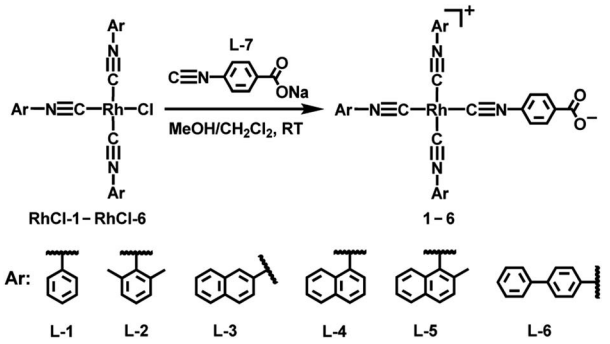

Scheme 1 Synthetic procedure of isocyanorhodium(I) zwitterions ([Rh(C≡N-aryl)$_3$(C≡N-4-benzoate)], **1–6**).

Rh(I) interactions that are further promoted by π–π stacking interactions and the hydrophilic–hydrophobic effect. As a result, zwitterions **2** and **5** are identified to exhibit intense NIR-II luminescence bands at 1005 and 1120 (1210, shoulder) nm with high quantum yields, large Stokes shifts, and microsecond lifetimes in methanol–water mixed solvents, respectively. Upon encapsulation with DSPE-mPEG2000 to form polymer nanoparticles in water (**2**/**5-PN**), deeper NIR-II emissions are observed at 1070 and 1130 (1230, shoulder) nm. Moreover, **2**/**5-PN** can light up tumor issues in the NIR-II region *in vivo*. To the best of our knowledge, this work, for the first time, reported the square-planar d^8 metal complexes showcasing strong NIR-II phosphorescent emissions in solution.

Results and discussion

Design, synthesis, and characterization

As reported previously, the chloride ligand of neutral complexes [Rh(C≡N-aryl)$_3$Cl] could be replaced by the same arylisonitriles to yield the corresponding [Rh(arylisonitrile)$_4$]$^+$ complexes.[11] With this synthetic study in mind, we believed that the coordinated chloride in the neutral rhodium(I) complexes could be also exchanged by using a different isocyanide ligand having a negatively charged group. Such chloride-to-isocyanide metathesis reactions allowed us to develop asymmetric zwitterionic isocyanidorhodium(I) complexes. Here, a series of asymmetric zwitterions [Rh(C≡N-aryl)$_3$(C≡N-4-benzoate)] (**1–6**) were synthesized by the coordinating reactions of neutral precursors [Rh(C≡N-aryl)$_3$Cl] (**RhCl-1–RhCl-6**) with **L-7** (Scheme 1). These zwitterions contained a hydrophilic 4-isocyanobenzoate and a hydrophobic tris(arylisocyanido)rhodium(I) moiety, and were characterized by ^{1}H NMR spectra (Fig. S4–S9†), high-resolution electrospray ionization mass spectra (Fig. S16–S21†), Fourier transform infrared spectra (Fig. S22†), and elemental analyses.

Aggregation behavior in neat solvents

All the rhodium(I) zwitterions were soluble in methanol or dimethyl sulfoxide (DMSO), but did not dissolve in water, acetonitrile, or tetrahydrofuran. The dilute solutions of **1–6** in methanol or DMSO (5.0×10^{-5} mol L^{-1}) appeared light yellow. UV–vis absorption studies showed that intense absorption bands in the range of 338–355 nm were due to π → π* transitions of the arylisonitrile ligands, whereas weak absorption shoulders at 463–472 nm were assigned to 4dz^2(Rh) → 5pz(Rh) transitions mixing with metal-to-ligand charge transfer (MLCT, dz^2(Rh) → π*(isocyanide)) transitions (Fig. 1a, d, S23–S28 and Table S1†).[8] No lower-energy absorptions were observed in the dilute solutions and all zwitterions exhibited weak emissions at *ca.* 530 nm (Fig. S29 and Table S1†), indicative of monomeric species therein.

At a high concentration of 1.0×10^{-3} mol L^{-1}, the solution colors of **1–6** changed to brown yellow, reddish brown, brown, blackish green, dark blue, and brown, respectively (Fig. 1a, d and S23–S28†). To understand such drastic color changes, concentration-dependent UV–vis absorption studies were conducted. When the concentrations were above 1.0×10^{-4} mol L^{-1}, new lower-energy absorption bands appeared at 543–582 nm for **1–6** and at 685–745 nm for **2–6**. These two absorption bands deviated from Beer's law and were assigned to dimeric 4dσ*(Rh$_2$) → 5pσ(Rh$_2$)/π*(isocyanide) and trimeric 4dσ*(Rh$_3$) → 5pσ(Rh$_3$)/π*(isocyanide) transitions, respectively.[8a,c,9a,c] Correspondingly, the dimeric emissions of **2**, **4**, and **5** were observed at 707–745 nm under concentrated conditions (1.0×10^{-3} mol L^{-1}) (Fig. S30†).[8f] Unexpectedly, two NIR-II emission bands of **5** appeared at 1120 and 1215 nm in the DMSO solution (Fig. S30†), probably due to trimeric or oligomeric 4dσ*(Rh$_n$) → 5pσ(Rh$_n$)/π*(isocyanide) ($n \geq 3$) excited states. Such aggregation forms arose from extended Rh(I)⋯Rh(I) contacts and π–π stacking interactions.

To quantify the aggregation processes, the binding constants of the dimers and trimers were analysed with monomer–dimer and dimer–trimer equilibriums, respectively (Fig. 1b, c, e, f, and S23–S28†).[8c,f] Accordingly, two types of linear correlations of [Rh]/$(A_2)^{1/2}$ *versus* $A_2{}^{1/2}$ and A_3 *versus* $A_2{}^{3/2}$ were attained, where [Rh] was the total concentration of the monomeric zwitterions, A_2 was the dimeric absorbance at 543–582 nm, and A_3 was the trimeric absorbance at 685–745 nm. The resulting dimerization (K_d) and trimerization constants (K_t) are summarized in Table S2.† Most of the K_d values were in the range of 10^3–10^4 L mol^{-1}, similar to data reported for homoleptic tetrakis(isocyanido) rhodium(I) complexes.[8c,f] Of note was that the K_d values of **2** and **4** in methanol were on the order of 10^6 and 10^5 L mol^{-1}, respectively. The former was probably due to the six methyl groups in **2** leading to a much stronger solvophobic, protective effect for favorable Rh(I)⋯Rh(I) interactions, while the latter was associated with strong π–π stacking interactions. The K_t values for both **4** in methanol and **5** in DMSO were on the order of 10^3 L mol^{-1}, which were much higher than those of other zwitterions in methanol or DMSO and homoleptic tetrakis(isocyanido)rhodium(I) complexes in dichloromethane or acetonitrile (~10^2 L mol^{-1}).[8c,f] The high aggregation tendency of **4** and **5** in solution indicated that strong π–π interactions arising from larger π–planar ligands played a key role in promoting Rh(I)⋯Rh(I) contacts. Moreover, temperature-dependent UV–vis absorption studies showed an isodesmic growth mechanism involving a non-nucleated aggregation pathway (Fig. S31–S36 and Table S3†).[8f,12]

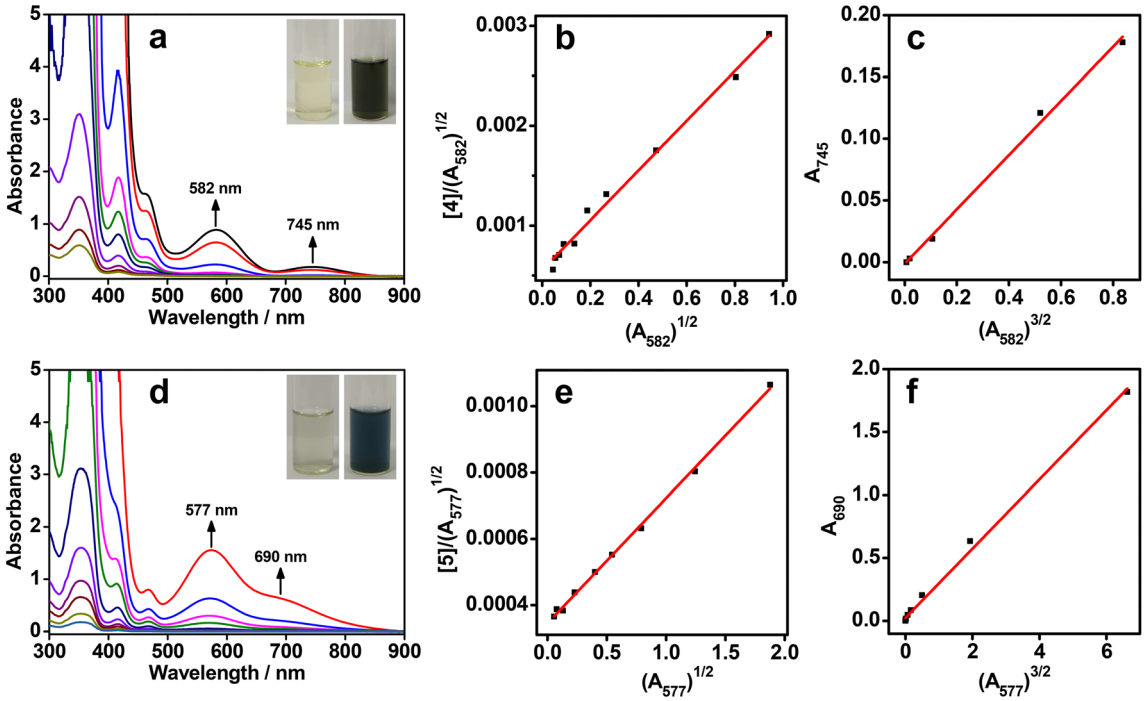

Fig. 1 Concentration-dependent UV-vis spectra of **4** in DMSO (a–c) and **5** in methanol (d–f) at room temperature. From bottom to top: (a) 5.0×10^{-5}, 6.0×10^{-5}, 7.0×10^{-5}, 8.0×10^{-5}, 1.0×10^{-4}, 2.0×10^{-4}, 4.0×10^{-4}, 8.0×10^{-4}, 1.0×10^{-3}, and 2.0×10^{-3} mol L^{-1}; (d) 3.0×10^{-5}, 4.0×10^{-5}, 5.0×10^{-5}, 6.0×10^{-5} 8.0×10^{-5}, 1.0×10^{-4}, 2.0×10^{-4}, 3.0×10^{-4}, 5.0×10^{-4}, and 1.0×10^{-3} mol L^{-1}. The dimerization (b and e) and trimerization (c and f) plots were obtained with monomer–dimer and dimer–trimer equilibriums by monitoring the dimeric and trimeric absorption bands, respectively. (Insets): The dilute solutions of **4** in DMSO and **5** in methanol (5.0×10^{-5} mol L^{-1}) were light yellow, while at a high concentration of 1.0×10^{-3} mol L^{-1}, the solutions changed to blackish green (a) and dark blue (d), respectively.

Concentration and temperature-dependent ^{1}H NMR spectra were obtained to corroborate the aggregation behaviors in solution (Fig. S37–S48 and Table S4†). Benefiting from strong π–π interactions from naphthalenes, large upfield shifts of aromatic proton resonances and association constants (K_a) were obtained for zwitterions **4** and **5**. In contrast, small upshifts and K_a values were captured for other zwitterions, suggestive of weak π–π stacking interactions appearing in solution. Altogether, the large binding constants of **2**, **4**, and **5** were consistent with the presence of NIR-I/II luminescence in their high-concentration solutions as a result of enhanced Rh(I)···Rh(I) interactions.

Solvent-induced supramolecular aggregation and NIR-II phosphorescence

The strong aggregation propensity of the rhodium(I) zwitterions, together with their NIR-I/II emissions in methanol and/or DMSO at high concentrations, urged us to further screen the availability of NIR-II luminescence by varying solvent compositions under dilute conditions (Fig. S49†). The screening results showed that the zwitterions of **2** and **5** exhibited distinctive color changes in methanol–water mixed solvents and the solutions remained stable for weeks (1.0×10^{-4} mol L^{-1}). Upon increase of the water content in the methanol solution of **2**, the solution color changed from pale yellow (100% methanol) to purple (50% methanol–water) and finally to blue (90–99% water, Fig. 2a). The difference was that the solutions of **5** showed a color variation from pale yellow (100% methanol) through blue (20% water) to green (beyond 50% water, Fig. 2b). Such solvatochromic trends were monitored by using UV–vis absorption and emission spectra. On increasing the water content, the dimeric absorption band of **2** at 546 nm grew gradually in intensity and red-shifted to 635 nm that was assigned to a 4dσ*(Rh_3) → 5pσ(Rh_3)/π*(isocyanide) transition (Fig. 2c). In the case of **5**, the trimeric absorption at 696 nm was found to exhibit a remarkable red shift to 790 nm concomitantly with a steady increase in intensity (Fig. 2g). The lower-energy absorption at 790 nm was assigned to a 4dσ*(Rh_n) → 5pσ(Rh_n)/π*(isocyanide) ($n > 3$) transition of oligomers arising from extended Rh(I)···Rh(I) interactions. Synchronously with these absorption changes in the low-energy regime, the high-energy π → π* absorptions showed large red shifts from 338 to 359 nm for **2** and from 353 to 382 nm for **5** with a significant drop in intensity, and the absorptions at *ca.* 413 and 463 nm featuring monomeric zwitterions disappeared completely. All these spectral results were indicative of a complete conversion from monomeric to trimeric species through a dimeric intermediate for **2** and to oligomeric species through dimeric/trimeric intermediates for **5**, respectively. Moreover, the solvent-induced assembly processes of **2** and **5** were found to follow an isodesmic aggregation mechanism by analysing the absorption spectral data with a solvent-dependent equilibrium model (Fig. 2d, h and Table S5†).[8f,13] Fitting of this model yielded Gibbs free energy changes (ΔG°) of −37.07 kJ mol^{-1} for **2**

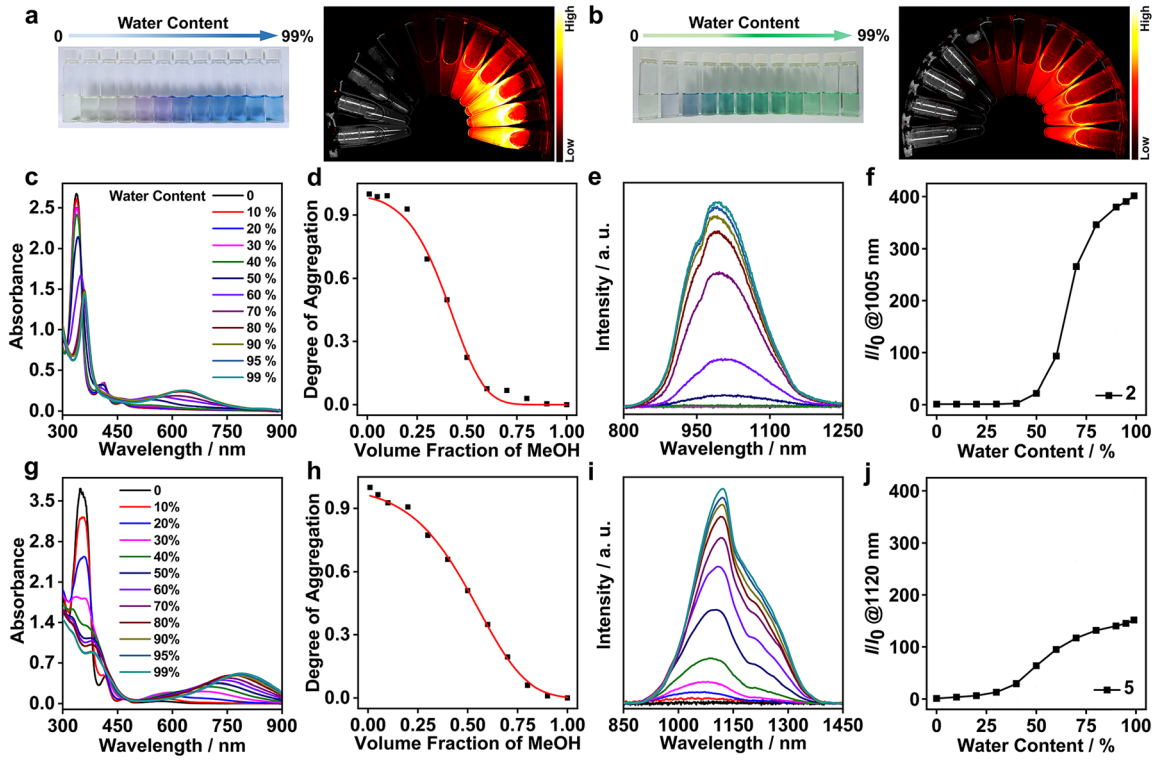

Fig. 2 Solutions of **2** (a) and **5** (b) in methanol–water solvent mixtures and their respective NIR-II luminescence images (percentage of water from left to right: 0, 10, 20, 30, 40, 50, 60, 70, 80, 90, 95, and 99%, 1.0×10^{-4} mol L^{-1}). UV–vis absorption spectra of **2** (c) and **5** (g) on increasing the water content in methanol. Plots of the normalized degree of aggregation of **2** (d) and **5** (h) at 635 and 790 nm against the methanol volume fraction were fitted according to the nucleation elongation aggregation model, typical of an isodesmic growth mechanism. Emission spectra of **2** (e) and **5** (i) showed strong NIR-II luminescence bands maximized at 1005 and 1120 nm, respectively. Plots of relative luminescence intensity of **2** (f) and **5** (j) at 1005 and 1120 nm *versus* the water volume fraction.

and −35.01 kJ mol^{-1} for **5**, due to enhanced Rh(I)···Rh(I) and π–π stacking interactions and the hydrophilic–hydrophobic effect on increasing the water content.

Upon photoexcitation at 635 nm, the NIR-II emission band of **2** at 1005 nm showed a steady increase in intensity when the water content was beyond 60%, and its maximum value was achieved at 90–99% water contents (Fig. 2e and f). Compared with **2**, **5** displayed a deeper NIR-II emission at 1120 nm together with a shoulder at 1220 nm with the increase of the water content up to 99% (Fig. 2i and j). The emission intensity of **2** at 1005 nm and **5** at 1120 nm was 360 and 150-fold higher than that in methanol, respectively, demonstrating controllable NIR-II luminescence enhancements through the solvent-induced strategy. Such spectral changes were coherent with those of the aforementioned absorption studies in methanol–water mixed solvents. Collectively, these two NIR-II emissions were assigned to $^3[4d\sigma^*(Rh_n) \rightarrow 5p\sigma(Rh_n)/\pi^*(\text{isocyanide})$, $n = 3$ and >3] excited states stemming from extended Rh(I)···Rh(I) contacts. Meanwhile, **2** and **5** possessed large Stokes shifts (370 (5798 cm^{-1}) and 330 nm (3730 cm^{-1})), high quantum yields (6.52% and 2.81%), and microsecond lifetimes (Table 1 and Fig. S50†). Therefore, we believed that the NIR-II emissions at 1005 nm for **2** and 1120 nm (1220, shoulder) for **5** were phosphorescent in nature.[14] It was interesting to note that zwitterion **5** was the first rhodium(I) complex showcasing strong NIR-II phosphorescent emissions centered at >1100 nm.

To unravel the supramolecular aggregation behind such excellent NIR-II phosphorescent properties, ^{1}H NMR studies were carried out at various CD_3OD–D_2O compositions (Fig. S51†). In pure CD_3OD, both of the zwitterions showed well-resolved proton signals. Upon increasing the water composition to 30%, both the aromatic and methyl proton signals were found to be gradually upfield shifted and broadened. The extent of the upfield shifts and broadening was more prominent in **5** than in **2** under the same solvent conditions, suggestive of stronger π–π stacking interactions and hydrophilic–hydrophobic effects in the former case. Further support for the aggregation came from zeta potential studies (Fig. S52†). The zeta potentials of **2** and **5** became increasingly negative as the water content increased in methanol, consistent with the increase in the hydrophilic–hydrophobic effect. Much more negative zeta potentials obtained at high water contents suggested that hydrophilic **L-7** was exposed on the outer surface of the aggregates, while the hydrophobic tris(arylisocyanido)rhodium(I) moieties were encapsulated inside.

Transmission electron microscopy (TEM) was used to investigate morphological changes in **2** and **5** during the solvent-induced aggregation process. It was found that changing the water content can lead to the morphology

Table 1 Photophysical properties of **2**, **5**, **2-PN**, and **5-PN**

Sample	λ_{max}/nm		Stokes shift/nm (cm^{-1})	Φ/%	Lifetime/μs	
	Absorption	Emission			$\tau_1{}^c$ (RW_1/%)	$\tau_2{}^c$ (RW_2/%)
2-99%[a]	635	1005	370 (5798)	6.52	1.41 (37.46)	12.25 (62.54)
5-99%[a]	790	1120 (sh, 1210)	330 (3730)	2.81	1.40 (31.04)	12.35 (68.96)
2-PN[b]	685	1070	385 (5253)	5.12	1.49 (29.13)	12.35 (70.87)
5-PN[b]	810	1130 (sh, 1230)	320 (3496)	3.20	1.50 (31.78)	11.64 (68.22)

[a] Measured in the methanol–water mixed solvent (v/v = 1/99) for **2** and **5**. [b] Measured in PBS for **2-PN** and **5-PN**. [c] Relative weighing (RW) of components in double exponential fits.

transformation of **5** from nanofibers (20–40% H_2O) into nanoparticles (99% H_2O) (Fig. 3a, b, d and S53†). Selected area electron diffraction (SAED) studies on the nanofibers (40% water, Fig. 3a) and nanoparticles (99% water, Fig. 3b) showed diffraction rings with spacings of 0.34 and 0.32 nm, indicative of the presence of Rh(I)···Rh(I) and π–π stacking interactions. The width of the nanofibers and the diameter of the nanoparticles were 32 ± 6.5 and 95 ± 15 nm, respectively. The difference was that **2** self-assembled into worms or networks of worms (60–80% water) and spherical nanoparticles (90% water, Fig. S54†). Conclusively, the aggregates of **2** and **5** showed a clear decrease in size on increasing the water content. This trend was further corroborated by dynamic light scattering (DLS) examinations, where hydrodynamic diameters (D_hs) of both **2** and **5** decreased on increasing the water content (Fig. S55†).

However, on this aggregate level, we cannot get insight into the details of molecular arrangements and local contacts. For this purpose, 2D ^1H–^1H NOESY NMR experiments for **2** and **5** were performed to elucidate their stacking modes in the supramolecular aggregates (Fig. 3c and S56†). The resulting NOESY NMR spectrum of **5** in the CD_3OD–D_2O (v/v = 9/1) solvent mixture showed three NOE signals featuring a through-space correlation between H_h (7.80 ppm) and H_d (7.40 ppm), H_a (7.87 ppm) and H_i (7.17 ppm), and H_i (7.17 ppm) and H_g (2.44 ppm, Fig. 3c). The relative integrals of the cross-peak signals allowed an estimation of the intermolecular distances of 2.63–3.16 Å. For **2**, two NOE signals were observed between the methyl protons on **L-2** (H_c, 2.44 ppm) and the aromatic protons on **L-7** (H_h, 7.99 ppm and H_i, 7.53 ppm, Fig. S56†) with intermolecular distances of 3.00–3.18 Å. These NOESY NMR results suggested that both **2** and **5** adopted head-to-tail stacking modes with a local twist (Fig. 3d), and were supportive of the presence of π–π stacking interactions between the zwitterionic planes.

To substantiate the Rh(I)···Rh(I) contacts and π–π stacking interactions in the molecular arrangements of aggregates, the methanol–water solutions of **2** and **5** (1.0×10^{-4} mol L^{-1}) were further subjected to wide-angle X-ray scattering (WAXS) measurement.[2h,10] The solutions of **2** with 60% and 99% water exhibited strong WAXS signals at $2\theta = 25.64°$ and 27.79°, corresponding to the Rh(I)···Rh(I) and π–π distances of 3.47 and

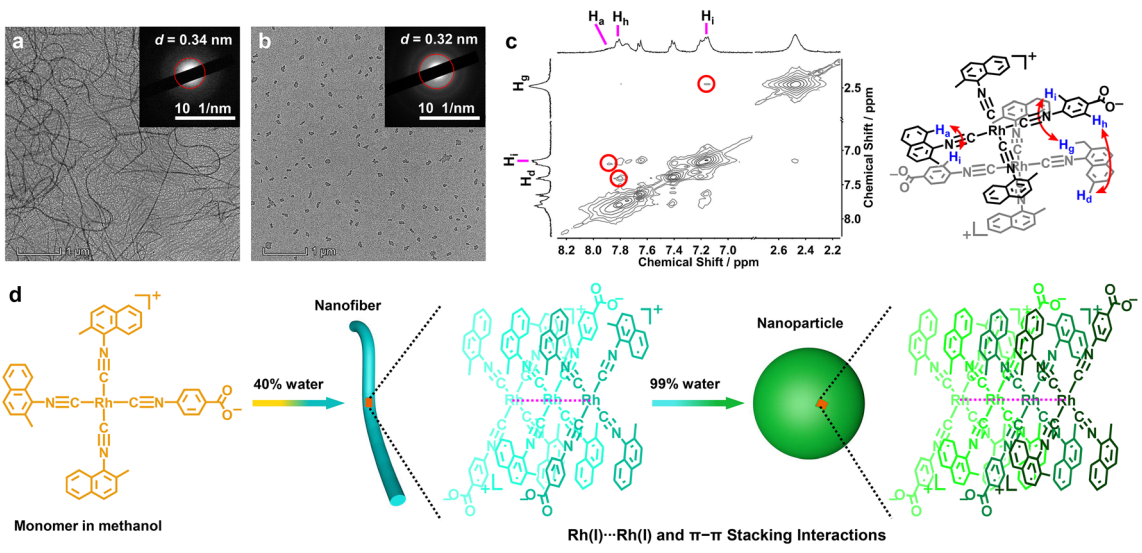

Fig. 3 TEM and SAED images of **5** obtained in the methanol–water mixed solvents with 40% (a) and 99% water (b). (c) ^1H–^1H NOESY spectrum of **5** in the CD_3OD–D_2O solvent mixture (v/v = 9/1, 2.0×10^{-3} mol L^{-1}, 400 MHz, 298 K). (d) Schematic illustration of the evolution of supramolecular aggregation into nanofibers and nanoparticles *via* extended Rh(I)···Rh(I) and π–π stacking interactions and the hydrophilic–hydrophobic effect on increasing the water content.

3.21 Å, respectively (Fig. 4a). In the case of **5**, intense WAXS bands were observed at $2\theta = 25.94°$ (3.43 Å, 40% water) and 28.56° (3.12 Å, 99% water, Fig. 4b). The latter was shorter than that in **2**, suggestive of stronger Rh(I)···Rh(I) and π–π stacking interactions in **5**. Moreover, the spacings of 3.21 and 3.12 Å were comparable to those Rh(I)···Rh(I) separations (3.07–3.29 Å) found in the crystal structures of homoleptic tetrakis(isocyanido)rhodium(I) complexes.[8c,d,f,i] Taking into account all these lines of evidence, we believed that the NIR-II phosphorescence enhancements of **2** and **5** were due to the increasing Rh(I)···Rh(I) interactions promoted by π–π stacking interactions and the hydrophilic–hydrophobic effect, and the deeper NIR-II emission of **5** should be attributed to closer Rh(I)···Rh(I) contacts therein.

NIR-II phosphorescence imaging

Having identified **2** and **5** as excellent NIR-II luminophores and elucidated their underlying luminescence mechanism, we then constructed **2**/**5**-containing polymer nanoparticles (**2-PN** and **5-PN**) in phosphate-buffered saline (PBS, pH = 7.4) by using nanoprecipitation with DSPE-mPEG2000 for phosphorescence bioimaging. The aqueous solutions of **2-PN** (sea blue) and **5-PN** (green) exhibited moderately intense low-energy absorptions at 685 and 810 nm, which showed red shifts of 50 and 20 nm as compared to **2** and **5** at 99% water, respectively (Fig. 5a, b and Table 1). Correspondingly, the emission bands were red shifted to 1070 and 1130 (1230, shoulder) nm with high Φ values, large Stokes shifts, and microsecond lifetimes (Table 1 and Fig. S50†). With reference to the spectroscopic studies of **2** and **5**, the red-shifted absorption and emission bands of **2-PN** and **5-PN** were assigned to $4d\sigma^*(Rh_n) \rightarrow 5p\sigma(Rh_n)/\pi^*$(isocyanide) ($n > 3$) transitions, which could be ascribed to the formation of higher oligomers through extended Rh(I)···Rh(I) and π–π stacking interactions and the hydrophilic–hydrophobic effect in the polymer nanoparticles. The aqueous solutions of **2-PN** and **5-PN** exhibited strong WAXS signals at $2\theta = 27.86°$ (3.20 Å) and 28.05 (3.18 Å), respectively (Fig. S57†), representing strong Rh(I)···Rh(I) and π–π stacking interactions. TEM studies demonstrated that **2-PN** exhibited a rice-like morphology with an average size of *ca.* 80 × 40 nm^2 (Fig. 5c and e), and **5-PN** appeared as spherical aggregates with a diameter of *ca.* 90 nm (Fig. 5d and f). The DLS plots of **2-PN** and **5-PN** revealed D_hs of 90 and 105 nm with uniform size distributions, respectively (Fig. 5g). Meanwhile, **2-PN** and **5-PN** in water showed zeta potentials of −11.5 mV and −17.2 mV, respectively, consistent with those of nanoparticles consisting of PEG as the corona (Fig. 5g).[10]

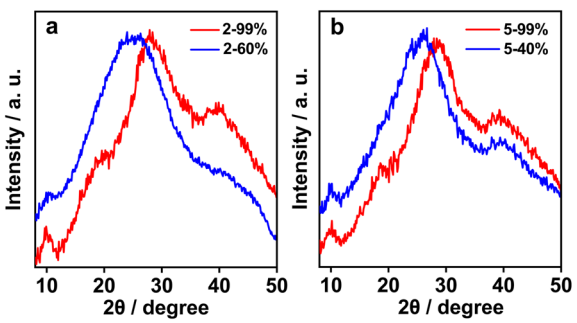

Fig. 4 WAXS patterns of (a) **2** with 60% and 99% water and (b) **5** with 40% and 99% water in methanol at 1.0×10^{-4} mol L^{-1}.

Next, the cytotoxicity of **2-PN** and **5-PN** was evaluated *in vitro* in human cancer and normal cell lines by standard MTT assay (Fig. S58, S59 and Table S6†). The results showed that both of the nanoparticles resulted in significant cytotoxicity on the human hepatoma Bel-7404 cell line. The half-maximal inhibitory concentrations (IC_{50}) of **2-PN** and **5-PN** were determined to be 2.6×10^{-5} and 4.3×10^{-5} mol L^{-1} at an incubation period of 24 h, which further decreased to 1.0×10^{-5} and 2.0×10^{-5} mol L^{-1} at 48 h, respectively. Interestingly, much higher IC_{50} values were observed for both **2-PN** and **5-PN** in the normal L02 cell line, suggestive of a low side effect on the normal cells. Then, the dose-dependent toxicity was evaluated by administering **2-PN** or **5-PN** *via* tail intravenous injection at various doses in a mouse model (Fig. S60†). The results showed a tolerable dosage of 10.0 mg kg^{-1} for both **2-PN** and **5-PN**, and higher dosages resulted in acute toxicity and thus, mouse mortality. Finally, the *in vivo* toxicity of **2-PN** and **5-PN** was assessed by performing biochemical measurements of liver (ALT and AST), heart (CK and CK-MB), and kidney (BUN and CR) levels (Fig. S61†). Minimal differences were observed between the groups treated with PBS, **2-PN**, or **5-PN**, suggesting that neither **2-PN** nor **5-PN** caused any detrimental effects on the heart, kidney, or liver of the treated mice. Additionally, as depicted in Fig. S62,† the blood routine examination parameters and hepatic/renal function indicators indicated no noticeable difference among the groups treated with PBS, **2-PN**, or **5-PN**, suggesting that both **2-PN** and **5-PN** possessed good biosafety.

Both superior NIR-II phosphorescence and biosafety inspired us to further explore the utilization of **2**/**5-PN** as bioimaging agents *in vivo*. The polymer nanoparticles were then introduced into Bel-7404-tumor-bearing nude mice by tail intravenous injection to perform NIR-II phosphorescence imaging at different time points (Fig. 6a). The resulting luminescence intensity was quantitatively monitored in the nude mice (Fig. 6b). As shown in Fig. 6a and b, both **2-PN** and **5-PN** lit up the tumor area in the NIR-II luminescence window after the injection, wherein the luminescence intensities reached maximum values at 24 h. Afterwards, the luminescence signals exhibited a gradual decrease in intensity, due to the natural metabolism of the polymer nanoparticles. Then, the mice were sacrificed at 72 h after administration to collect major organs (heart, liver, spleen, lung, and kidney) and tumors for further NIR-II luminescence imaging studies (Fig. 6c and d). The results showed that both the liver and tumor areas showed strong luminescence signals, while almost no such signals were observed for the other major organs. To elaborate the metabolism process of **2-PN** and **5-PN**, the content of Rh atoms in the tumors and normal tissues was analyzed by inductively coupled plasma-mass spectrometry (ICP-MS) (Fig. S63†). Compared with other major organs, the significant accumulations of Rh in the livers and tumors were observed clearly, which were consistent with the aforementioned NIR-II luminescence imaging results.

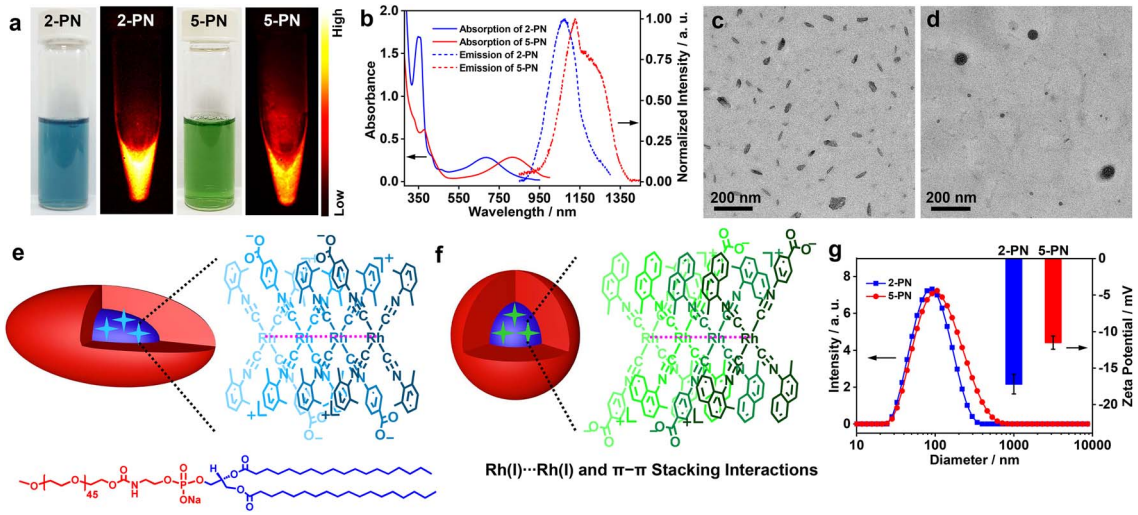

Fig. 5 (a) Sea blue and green solutions and NIR-II luminescence images of **2-PN** and **5-PN**. (b) Their UV–vis absorption and emission spectra in PBS (1.2×10^{-4} mol L^{-1}). TEM images and schematic illustrations of **2-PN** (c and e) and **5-PN** (d and f). (g) DLS plots and zeta potential data of the polymer nanoparticles.

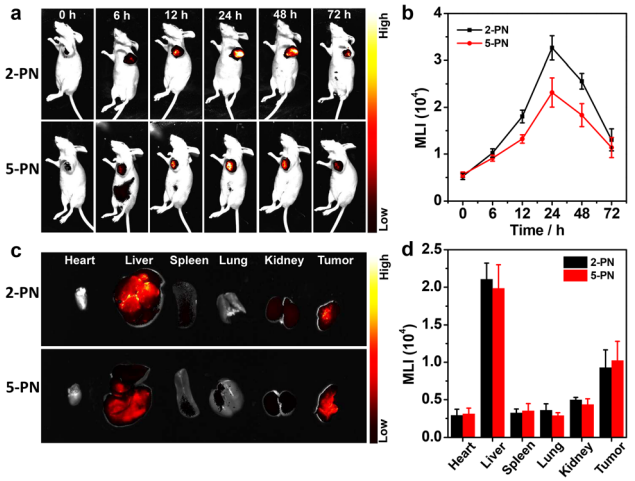

Fig. 6 (a) *In vivo* NIR-II phosphorescence bioimaging of Bel-7404-tumor-bearing nude mice at various time points after the intravenous administration of **2-PN** and **5-PN**. (b) The mean luminescence intensity (MLI) values of **2-PN** and **5-PN** at different time points. (c) The corresponding phosphorescence bioimaging of the resected tumors and organs at 72 h. (d) The MLI values in the tumor and normal tissues at 72 h after the injection of **2-PN** and **5-PN**.

Consequently, both the time-lapse imaging and ICP-MS studies showed that **2**/**5-PN** evolved *in vivo* to mainly accumulate into liver and tumor areas, which were associated with the metabolic pathway and enhanced permeability and retention (EPR) effect of the nanoparticles,[15] respectively.

All of the treated mice were found to show negligible body weight changes, indicative of the high biocompatibility and low systematic toxicity of these two nanoparticles (Fig. S64†). The tumor organs were further sliced and stained with hematoxylin and eosin (H&E) for histological analyses. Compared with the control group, the tumor slices showed typical features of cancer cell apoptosis, such as shrinkage and fragmentation in nuclei in both the cases of **2-PN** and **5-PN** (Fig. S65a†). Meanwhile, **2-PN** exhibited much more serious apoptosis than **5-PN**, which was further confirmed by immunohistochemical analyses (Fig. S65b†). Additional histological analyses of the main organs (heart, liver, spleen, lung, and kidney) did not show any recognizable pathological alterations or other abnormalities (Fig. S66†), suggestive of the excellent biocompatibility and biosafety of the nanoparticles.[16]

Conclusions

We have developed a promising asymmetric coordination paradigm to create arylisocyanidorhodium(I) zwitterions, [Rh(C≡N-aryl)$_3$(C≡N-4-benzoate)] (**1–6**). By varying their concentration, temperature, and solvent composition, these zwitterions are found to show strong aggregation propensity as a result of extensive Rh(I)···Rh(I) interactions promoted by π–π stacking and hydrophilic–hydrophobic interactions. As such, **2** and **5** show NIR-II phosphorescence emissions at 1005 and 1120 (1210, shoulder) nm in methanol–water mixed solvents, which can be further red-shifted to 1070 and 1130 (1230, shoulder) nm for their polymer nanoparticles in water (**2**/**5-PN**), respectively. However, the resulting polymer nanoparticles can brighten *in vivo* tumor issues in the NIR-II region. This work offers a novel insight into the design of NIR-II phosphorescent materials.

Ethical statement

All experimental designs and protocols involving animals were approved by the Experimental Animal Ethics Committee of the University of South China, Hunan, People's Republic of China (approval 4304079008946), and complied with the National Institutes of Health and University of South China guidelines on the care and use of animals for scientific purposes.

Data availability

Data is included in ESI.†

Author contributions

W. Bu, J. Wang, and W. Wei conceived the idea, designed the experiments and co-wrote the manuscript. W. Wei predominantly performed the preparation and characterization studies of all isocyanorhodium(I) zwitterions and the polymer nanoparticles, and their supramolecular aggregation and NIR-I/II luminescence studies with the assistance of X. Kang, H. Li, G. Chang and Q. He. All related biological studies were completed by J. Wang. W. Bu supervised the project and revised the manuscript. All authors were involved in the finalization of the manuscript.

Conflicts of interest

There are no conflicts to declare.

Acknowledgements

This work was supported by the National Natural Science Foundation of China (Grants 52073130, 92161126, and 22101127), Science and Technology Program of Gansu Province (22YF7WA015, 21JR7RA468 and 20JR5RA057), the Science and Technology Project of Hunan Province (2021RC2084), and the Open Projects of State Key Laboratory of Environment-friendly Energy Materials (No. 20kfhg15) and State Key Laboratory of Supramolecular Structure and Materials of Jilin University (sklssm202303).

Notes and references

1 (*a*) T. F. A. de Greef and E. W. Meijer, *Nature*, 2008, **453**, 171; (*b*) L. Brunsveld, B. J. B. Folmer, E. W. Meijer and R. P. Sijbesma, *Chem. Rev.*, 2001, **101**, 4071; (*c*) F. Huang and O. A. Scherman, *Chem. Soc. Rev.*, 2012, **41**, 5879; (*d*) G. V. Oshovsky, D. N. Reinhoudt and W. Verboom, *Angew. Chem., Int. Ed.*, 2007, **4**, 2366; (*e*) I. V. Kolesnichenko and E. V. Anslyn, *Chem. Soc. Rev.*, 2017, **46**, 2385.

2 (*a*) Q. Wan, X.-S. Xiao, W.-P. To, W. Lu, Y. Chen, K.-H. Low and C.-M. Che, *Angew. Chem., Int. Ed.*, 2018, **57**, 17189; (*b*) Q. Gao, F. Peng, C. Wang, J. Lin, X. Chang, C. Zou and W. Lu, *Chin. J. Chem.*, 2021, **39**, 1159; (*c*) V. C.-H. Wong, C. Po, S. Y.-L. Leung, A. K.-W. Chan, S. Yang, B. Zhu, X. Cui and V. W.-W. Yam, *J. Am. Chem. Soc.*, 2018, **140**, 657; (*d*) Y.-S. Wong, M. Ng, M. C.-L. Yeung and V. W.-W. Yam, *J. Am. Chem. Soc.*, 2021, **143**, 973; (*e*) J. Li, K. Chen, J. Wei, Y. Ma, R. Zhou, S. Liu, Q. Zhao and W.-Y. Wong, *J. Am. Chem. Soc.*, 2021, **143**, 18317; (*f*) M. H.-Y. Chan, S. Y.-L. Leung and V. W.-W. Yam, *J. Am. Chem. Soc.*, 2019, **141**, 12312; (*g*) C. Po, A. Y.-Y. Tam, K. M.-C. Wong and V. W.-W. Yam, *J. Am. Chem. Soc.*, 2011, **133**, 12136; (*h*) W. Meng, Q. He, M. Yu, Y. Zhou, C. Wang, B. Yu, B. Zhang and W. Bu, *Polym. Chem.*, 2019, **10**, 4477.

3 (*a*) Q. Wan, W.-P. To, X. Chang and C.-M. Che, *Chem*, 2020, **6**, 945; (*b*) Q. Wan, W.-P. To, C. Yang and C.-M. Che, *Angew. Chem.*, 2018, **130**, 3143; (*c*) K. K. Kartha, N. K. Allampally, A. T. Politi, D. D. Prabhu, H. Ouchi, R. Q. Albuquerque, S. Yagai and G. Fernández, *Chem. Sci.*, 2019, **10**, 752.

4 (*a*) Q. Wan, J. Xia, W. Lu, J. Yang and C.-M. Che, *J. Am. Chem. Soc.*, 2019, **141**, 11572; (*b*) V. W.-W. Yam, V. K.-M. Au and S. Y.-L. Leung, *Chem. Rev.*, 2015, **115**, 7589.

5 (*a*) G.-Q. Jin, D.-e. Sun, X. Xia, Z.-F. Jiang, B. Cheng, Y. Ning, F. Wang, Y. Zhao, X. Chen and J.-L. Zhang, *Angew. Chem., Int. Ed.*, 2022, **61**, e202208707; (*b*) Y. Xu, C. Li, S. Lu, Z. Wang, S. Liu, X. Yu, X. Li and Y. Sun, *Nat. Commun.*, 2022, **13**, 2009; (*c*) Y. Fan, C. Li, S. Bai, X. Ma, J. Yang, X. Guan and Y. Sun, *Small*, 2022, **18**, 2201625; (*d*) Y. Qin, X. Chen, Y. Gui, H. Wang, B. Z. Tang and D. Wang, *J. Am. Chem. Soc.*, 2022, **144**, 12825; (*e*) N. Sinha, J.-R. Jiménez, B. Pfund, A. Prescimone, C. Piguet and O. S. Wenger, *Angew. Chem., Int. Ed.*, 2021, **60**, 23722.

6 J.-C. G. Bünzli and S. V. Eliseeva, *J. Rare Earths*, 2010, **28**, 824.

7 S. Addankia, I. S. Amirib and P. Yupapin, *Results Phys.*, 2018, **10**, 743.

8 (*a*) K. R. Mann, J. G. Gordon and H. B. Gray, *J. Am. Chem. Soc.*, 1975, **97**, 3553; (*b*) V. M. Miskowski, G. L. Nobinger, D. S. Kliger, G. S. Hammond, N. S. Lewis, K. R. Mann and H. B. Gray, *J. Am. Chem. Soc.*, 1978, **100**, 485; (*c*) K. R. Mann, N. S. Lewis, R. M. Williams, H. B. Gray and J. G. Gordon, *Inorg. Chem.*, 1978, **17**, 828; (*d*) N. T. Tran, J. R. Stork, D. Pham, M. M. Olmstead, J. C. Fettinger and A. L. Balch, *Chem. Commun.*, 2006, 1130; (*e*) Y. Chen, K. Li, H. O. Lloyd, W. Lu, S. S.-Y. Chui and C.-M. Che, *Angew. Chem., Int. Ed.*, 2010, **49**, 9968; (*f*) A. K.-W. Chan, K. M.-C. Wong and V. W.-W. Yam, *J. Am. Chem. Soc.*, 2015, **137**, 6920; (*g*) V. Conejo-Rodríguez, B. Donnio, B. Heinrich, R. Termine, A. Golemme and P. Espinet, *J. Mater. Chem. C*, 2023, **11**, 1435; (*h*) L. T.-L. Lo, W.-K. Chu, C.-Y. Tam, S.-M. Yiu, C.-C. Ko and S.-K. Chiu, *Organometallics*, 2011, **30**, 5873; (*i*) N. T. Tran, J. R. Stork, D. Pham, C. J. Chancellor, M. M. Olmstead, J. C. Fettinger and A. L. Balch, *Inorg. Chem.*, 2007, **46**, 7998.

9 (*a*) V. M. Miskowski, S. F. Rice, H. B. Gray, R. F. Dallinger, S. J. Milder, M. G. Hill, C. L. Exstrom and K. R. Mann, *Inorg. Chem.*, 1994, **33**, 2799; (*b*) C.-M. Che, W.-M. Lee, H.-L. Kwong, V. W.-W. Yam and K.-C. Cho, *J. Chem. Soc., Dalton Trans.*, 1990, 1717; (*c*) J. J. Stace, K. D. Lambert, J. A. Krause and W. B. Connick, *Inorg. Chem.*, 2006, **45**, 9123.

10 J. Wang, J.-J. Nie, P. Guo, Z. Yan, B. Yu and W. Bu, *J. Am. Chem. Soc.*, 2020, **142**, 2709.

11 Y. Yamamoto, K. Aoki and H. Yamazaki, *Inorg. Chem.*, 1979, **18**, 1681.

12 (*a*) L. Li, N. Zhou, H. Kong and X. He, *Polym. Chem.*, 2019, **10**, 5465; (*b*) A. K.-W. Chan, M. Ng, K.-H. Low and V. W.-W. Yam, *J. Am. Chem. Soc.*, 2018, **140**, 8321; (*c*) A. K.-W. Chan, D. Wu, K. M.-C. Wong and V. W.-W. Yam, *Inorg. Chem.*, 2016, **55**, 3685.

13 (*a*) P. A. Korevaar, C. Schaefer, T. F. A. de Greef and E. W. Meijer, *J. Am. Chem. Soc.*, 2012, **134**, 13482; (*b*) J. Matern, K. K. Kartha, L. Sánchez and G. Fernández,

Chem. Sci., 2020, **11**, 6780; (*c*) N. Zhou, R. Hailes, Y. Zhang, Z. Chen, I. Manners and X. He, *Polym. Chem.*, 2020, **11**, 2700.

14 (*a*) E. R. Sauvé, C. M. Tonge and Z. M. Hudson, *J. Am. Chem. Soc.*, 2019, **141**, 16422; (*b*) N. Wu, H. Xiao, Y. Lou, M. Han, Z. Guo and H. Zhan, *J. Phys. Chem. C*, 2021, **125**, 22848.

15 (*a*) E. Blanco, H. Shen and M. Ferrari, *Nat. Biotechnol.*, 2015, **33**, 941; (*b*) J. Wang, W. Mao, L. L. Lock, J. Tang, M. Sui, W. Sun, H. Cui, D. Xu and Y. Shen, *ACS Nano*, 2015, **9**, 7195.

16 (*a*) K.-C. Tong, P.-K. Wan, C.-N. Lok and C.-M. Che, *Chem. Sci.*, 2021, **12**, 15229; (*b*) Y. Long, J. Chen, F. Zeng and S. Wu, *Aggregate*, 2023, **4**, e288; (*c*) R. Wang, C. Yin, C. Liu, Y. Sun, P. Xiao, J. Li, S. Yang, W. Wu and X. Jiang, *J. Am. Chem. Soc.*, 2021, **143**, 20927.